Research Square

Preprints are preliminary reports that have not undergone peer review. They should not be considered conclusive, used to inform clinical practice, or referenced by the media as validated information.

From Hard Carbon to Activated Carbon: Influence of Surface Area and Pore Structure on the Electrochemical Performance of Coconut Rachis-Derived Supercapacitor Electrodes

Devu Bindhu
Amrita Vishwa Vidyapeetham
M S Gayathri
Amrita Vishwa Vidyapeetham
Anju Ramachandran
Amrita Vishwa Vidyapeetham
Jinchu I
Goverment College Kottayam
Rajan Jose
Ming Chi University of Technology
C O Sreekala
sreekalaco@am.amrita.edu

Amrita Vishwa Vidyapeetham

Article

Keywords: Biomass-derived carbon, Hard carbon, Activated carbon, Electric double-layer capacitor (EDLC), Pore structure, Supercapacitor

Posted Date: September 4th, 2026

DOI: https://doi.org/10.21203/rs.3.rs-10727726/v1

License: This work is licensed under a Creative Commons Attribution 4.0 International License. Read Full License

Additional Declarations: No competing interests reported.

Version of Record: A version of this preprint was published at Scientific Reports on October 23rd, 2026. See the published version at https://doi.org/10.1038/s41598-026-76732-1.

Abstract

The performance of supercapacitors depends on the structural characteristics of electrode materials and their interactions with electrolytes. In the present work, hard carbon (HC) and chemically treated coconut rachis-derived activated carbon (AC) are comparatively studied for understanding the role of porosity, surface area and electrochemical performance. Through chemical activation, the compact structure of HC was converted to a hierarchically porous AC, resulting in an increased specific surface area from 32 to ~1025 $m^2 g^{-1}$. Such AC provided rich electrochemical active sites along with efficient transport of electrolyte ions. Structural and compositional changes induced by activation were characterised using FESEM, BET, EDX, XRD, FTIR, and Raman spectroscopy. Electrochemical performances of HC and AC were analysed using different aqueous electrolytes. In all electrolytes, AC showed better capacitive behaviour than HC due to the developed hierarchical pore system and high surface area. AC in 6 M KOH showed a maximum specific capacitance of 201 F g^{-1}. Besides, the supercapacitor assembled using AC in 6 M KOH showed a high specific capacitance with ~93% capacitance retention after 2000 cycles of charge-discharge. These findings demonstrate that engineering the pore structure and surface area of biomass-derived carbon is essential for enhancing supercapacitor performance.

1. Introduction

Energy demand across the globe has been increasing continuously in recent years due to the speeding up of industrialisation, urbanisation, and a growing population. This has made the need for an environmentally sustainable and secure supply of energy highly critical, especially since conventional fossil fuels are on the decline, with their detrimental environmental impact becoming apparent [1–4]. Sources of renewable energy, including solar and hydro power, have started becoming viable alternatives [5–9]. These energy sources, however, face difficulties with intermittency and storage efficiency.. Highlighting the very need for efficient storage technologies capable of storing and releasing energy in a precise manner to ensure a steady power supply after renewables are not available.

Traditional energy storage systems, including batteries, are being extensively used; however, they suffer from environmental hazards. Lithium-ion batteries bring about issues of material exhaustion, lack of recyclability, and dangerous waste disposal[10, 11]. Extraction of materials, such as lithium, cobalt, and nickel, causes destruction to the environment as well as human rights issues in certain locations. Also, batteries have short-life cycles and low power density as compared to other energy storage devices [12]. All these factors have brought about research for alternative energy storage devices, and among them are supercapacitors due to their numerous advantages.

Supercapacitors offer some decent advantages over conventional batteries, like a longer cycle life, high power density, and a faster charge-discharge rate[13–15]. In contrast to the batteries that create and discharge energy via different chemical processes, the supercapacitors generate energy electrostatically due to charge accumulation at the interface between the electrode and electrolyte charge, allowing fast

energy release and recharge. They quickly dissipate energy, thus making them suitable for situations when short bursts of energy are needed, such as electric vehicles, portable electronics, and grid stabilization[16, 17]. Furthermore, the supercapacitors are environmentally friendly since they use readily available and sustainable materials [18, 19]. Added to that, their longer life cycle provides a further decrease in the frequency with which they need to be replaced, making them yet another sustainable option.

Supercapacitor efficiency is highly influenced by the choice of materials used in the fabrication of the electrodes, which are made up of carbon materials due to high surface area, good electrical conductivity, chemical stability, and adjustable pores [20–23]. Biomass-derived hard carbon (HC) is one of such carbon materials that have gained much popularity due to its low cost, renewability, and stability. The problem with such pristine material is that it has relatively low specific surface area and restricted pores access, which affects its electrochemical efficiency. In order to address these challenges, a technique called chemical activation has been identified as one of the techniques that can effectively convert hard carbons into AC by developing large numbers of micro- and mesopores, enhancing the specific surface area, and making more electrochemically active sites available. This makes it possible to have electrolyte ions pass through at a much faster rate and store charges, making it ideal for use in supercapacitors[24, 25]. While significant efforts have been devoted to optimizing the structural and morphological properties of carbon-based electrode materials, the role of electrolyte parameters in governing electrochemical performance remains comparatively underexplored. In electrical double-layer capacitors, the process of energy storage is highly dependent on the interaction between electrolyte ions and the surface of the porous electrode. Key electrolyte parameters, related to the electrolyte, including the size of the electrolyte ions, ionic conductivity, concentration of the electrolyte, and solvation characteristics of the electrolyte, have an important effect on the ion transport mechanism and their ability to reach the active sites [26]. Understanding the combined influence of pore structure and electrolyte properties is therefore crucial for optimizing the electrochemical behaviour of biomass-derived carbon electrodes.

In the current study, the usage of hard carbon (HC) and activated carbon (AC) obtained from coconut rachis was used as electrode material to study the influence of structural features on the electrochemical performance. Characterization of physicochemical properties of HC and AC was done in terms of their capacitive performance in three types of alkaline electrolyte (6 M KOH, 6 M NaOH, and 6 M LiOH). Moreover, a symmetric supercapacitor cell was built with the use of AC to determine its practical energy storage performance. This work provides valuable insights into how the transformation of hard carbon into a high-surface-area activated carbon, together with the selection of a suitable electrolyte, governs the electrochemical performance of sustainable biomass-derived supercapacitor electrodes.

2. Experimental Procedure

2.1 Preparation of coconut rachis activated carbon

To synthesize activated carbon, coconut rachis, a biowaste material, was collected locally from Kollam, Kerala, India. The coconut rachis was first washed with DI water to eliminate impurities and then dried out under sunlight for 48 hours. After sun-drying, the sample was placed in a hot air oven for an additional 48 hours to eliminate any remaining moisture. To break down organic compounds such as cellulose and hemicellulose, the coconut rachis was annealed at 250°C for two hours. This pre-carbonized sample was then additionally annealed at 450°C for two hours under an inert atmosphere to break the lignin bonds, yielding HC from the coconut rachis. To enhance the properties of the synthesized HC, activation using a chemical activation agent, potassium hydroxide (KOH). KOH was mixed with the synthesized carbon in a 3:1 weight ratio and annealed at 600°C for 4 hours in a controlled atmosphere. After activation, the sample was cleaned carefully with DI water until the pH of the wash water became neutral. Finally, the activated carbon was dried in a hot air oven at 60°C overnight, resulting in the production of coconut rachis activated carbon.

2.2 Characterization techniques

The morphology of the synthesized HC and AC was characterized by scanning electron microscopy (SEM) using a JEOL JSM-IT200 microscope coupled with an Oxford Instruments JEOL LA6390LA energy-dispersive X-ray spectroscopy (EDS) system. The specific surface area and pore characteristics of the samples were determined by nitrogen adsorption–desorption analysis using a NOVA touch 4LX surface area and pore size analyzer (Anton Paar/Quantachrome Instruments), and the specific surface area was calculated using the Brunauer–Emmett–Teller (BET) method. Owing to its higher specific surface area, the crystallographic structure of the activated carbon was analyzed by powder X-ray diffraction (XRD) using a Rigaku MiniFlex II diffractometer with Cu Kα radiation over a 2θ range of 20–80°. The surface functional groups of the samples were analyzed using a Thermo Fisher Scientific Nicolet iS50 Fourier-transform infrared (FTIR) spectrometer. Raman spectroscopy was performed to investigate the structural characteristics and degree of graphitization of the carbon samples using a Renishaw Laser Confocal Raman Spectrometer with microscope attachment equipped with a 514 nm excitation laser.

2.3 Electrode and device fabrication

Working electrodes were fabricated using the prepared HC and AC as the active materials. The electrode slurry was prepared by mixing the active material, Super P conductive carbon, and polyvinylidene fluoride (PVDF) binder in a weight ratio of 8:1:1 using N-methyl-2-pyrrolidone (NMP) as the solvent. The homogeneous slurry was uniformly coated onto pre-cleaned nickel foam current collectors and dried overnight at 60°C.

Electrochemical measurements were carried out in a three-electrode configuration using the prepared HC or AC electrode as the working electrode, Ag/AgCl as the reference electrode, and a platinum mesh as the counter electrode. The electrochemical performance was evaluated in 6 M KOH, NaOH, and LiOH aqueous electrolytes. Cyclic voltammetry (CV) measurements were performed over a potential window of 0–1.0 V at scan rates ranging from 10 to 100 mV s^{-1}. Galvanostatic charge–discharge (GCD)

measurements were conducted within the same potential window at current densities of 1–10 A g^{-1}. Electrochemical impedance spectroscopy was applied to examine the charge transfer properties and the internal resistance of the electrode-electrolyte interface.

For performance evaluation, symmetrical supercapacitors were prepared utilizing AC as negative and positive electrodes, respectively, in Swagelok-type cell arrangement. Glass fiber membrane (Grade GF/D, Whatman®) was employed as the separator. The electrochemical performance of the fabricated capacitor, such as specific capacitance, power and energy density, was estimated by GCD analysis.

3. Results and Discussions

3.1 Physicochemical Analysis

Morphology of the prepared HC and AC derived from the coconut rachis was studied via FESEM, and the micrographs obtained are shown in Fig. 1(a&b). It is evident that there exist notable morphological differences between HC and AC, showing how chemical activation has led to the creation of a highly different structure. The HC sample exhibits a relatively compact and irregular carbon matrix with rough surfaces, fractured domains, and sparsely distributed surface cavities. Although carbonization removes a considerable fraction of the volatile constituents from the biomass precursor, the resulting structure remains comparatively dense with limited pore connectivity. The pores observed can mainly be explained by the thermal degradation of hemicellulose, cellulose, and lignin in pyrolysis, which causes the production of volatiles and hence the development of initial pores in the carbon skeleton. Nonetheless, without any chemical activation, the pores will be relatively independent in their operation, thus limiting the development of an interconnected porosity structure[27, 28]. In the case of KOH activation, there is a great change in morphology towards a hierarchical porous structure with interconnected pore networks. This process allows for controlled etching of the carbon matrix, resulting in a high level of pores and increasing porosity interconnection in the electrode. Consequently, it can be concluded that the activated carbon has an easily accessible porosity structure, which indicates the efficiency of KOH activation in controlling the properties of the biomass-derived carbon[29, 30]. A significant structural transformation from HC to AC will allow us to significantly increase the textural properties of the material. The hierarchical porous structure provides an increased electrochemically accessible surface area due to the increased number of active areas for ions absorption from the electrolyte. Such an architecture is also expected to contribute to the structural stability of the electrode by accommodating repeated ion adsorption and desorption during continuous charge–discharge cycling without significant structural degradation [31–33]. On the other hand, due to the higher density of the HC material structure, the ions will not be able to penetrate easily and effectively, thus making the active sites less functional. To quantitatively evaluate the structural evolution induced by KOH activation, the textural properties of HC and AC were further investigated using nitrogen adsorption–desorption analysis[34, 35].

The structural features of HC and AC have been studied through Brunauer-Emmett-Teller (BET) method for determination of the surface properties of the carbons in view of the effect of chemical activation on

them. The values of BET parameters are presented in Table 1. For HC, there was found a relatively small value of specific surface area (32 $m^2 g^{-1}$), total pore volume (0.027 $cm^3 g^{-1}$), and an average pore diameter (2.81 nm). After KOH activation, the specific surface area increased significantly up to 1025.43 $m^2 g^{-1}$, whereas the total pore volume became equal to 0.5685 $cm^3 g^{-1}$ and the average pore diameter was equal to 2.22 nm. The significant increase in surface area and pore volume indicates the efficiency of KOH activation for the formation of porous network structure in carbon. The formed mesoporous structure ensures sufficient electrochemical accessible sites and electrolyte ion diffusion, which are supposed to influence on the electrochemical behavior. The significant improvement in the textural parameters of AC is in agreement with the FESEM analysis, according to which chemical activation converts the dense HC into hierarchical porous structure. The considerable enhancement in surface area along with the increase in pore volume reveals the presence of sufficient adsorption sites and pore channels, both being beneficial for easy electrolyte impregnation and charge accumulation. Thus, the improved properties of the surface can be considered favorable for ion diffusion and electrochemical activity in concentrated alkaline electrolytes. The nitrogen adsorption-desorption isotherms of HC and AC are illustrated in Fig. 1(c-f). The HC material possessed a Type II adsorption isotherm without a clear hysteresis loop that revealed insufficient pore development and presence of mainly non-porous surface[36–38]. The N_2 adsorption-desorption isotherm for the AC is shown in Fig. 1(e). The isotherm shows a characteristic Type IV adsorption behaviour along with an obvious H3 hysteresis loop in the relative pressure range of P/P_0 ~ 0.40–0.99, implying that the material possesses a mesoporous structure developed through the process of KOH activation. The continuous rise in the nitrogen content with increasing relative pressures shows the capillary condensation phenomenon inside the interconnected mesopores. From the pore size distribution plot (Fig. 1(f)), it can be seen that the pores have been found to be distributed primarily in the range of 2–5 nm, which is consistent with the average pore diameter found from BET analysis. Such surface characteristics are expected to facilitate electrolyte penetration, increase the number of electrochemically accessible active sites, and promote efficient ion transport during electrochemical operation.

For a further understanding of the composition variations caused by KOH activation, the composition of HC and AC was determined through EDX analysis, and the corresponding plots are shown in Fig. 1(g&h). The composition of the HC was dominated by carbon (77.94 wt %), oxygen (16.27 wt %), chlorine (1.30 wt %), potassium (2.23 wt %), and calcium (2.23 wt %). As a result of the activation process, the percentage of carbon increased to 85.91 wt % while the percentage of oxygen, potassium, and calcium decreased to 12.65 wt %, 0.25 wt %, and 1.19 wt %, respectively. These results suggest that the activation process helped in purifying and enriching carbon composition, which will make the material a carbon-enriched structure[39, 40]. Such compositional modification is expected to improve the electrical conductivity of the electrode and contribute to enhanced electrochemical performance.

Table 1
Comparison of the surface properties of coconut rachis HC and AC with commercial activated carbon

Sample	S_{bet} ($m^2 \cdot g^{-1}$)	V_{total} ($cm^3 \cdot g^{-1}$)	Av. pore size (nm)	Ref
AC-C	~ 415	0.22	2.17	[41]
Coconut rachis- Carbon	~ 32	0.027	2.81	**This work**
Coconut rachis- AC	~ 1025.43	0.57	2.22	**This work**

The crystal structure of the HC and AC samples was studied by means of X-ray diffraction (XRD), and the results of XRD are given in Fig. 2(a &b) [22, 30]. Distinct crystalline diffraction peaks of the HC sample were recorded at 2θ = 28.38°, 40.65°, 58.56°, 66.52°, and 73.84° related to the (110), (200), (211), (310), and (301) planes of the crystal, respectively, indicating the development of tetragonal carbon (space group I4/mmm)[22, 42]. Following KOH activation, the sharp crystalline reflections were significantly diminished and replaced by wide diffraction peaks centred at ~ 25.64° and 43.20°, which correspond to the (002) and (100) planes of graphitic carbon. Broadening and the reduction of the maximum intensity are evidence of a reduced level of crystallinity due to the conversion from an ordered tetragonal structure of carbon to an amorphous carbon structure due to the chemical activation process. The reduction in crystallinity was observed due to the restructure of the material and formation of pores due to KOH activation, and this is in agreement with FESEM and BET analysis results, indicating that hierarchical porous carbon structure was successfully synthesized. Surface functional groups of HC and AC have been characterized using Fourier transform infrared (FTIR) spectroscopy, and FTIR spectra have been shown in Fig. 2c. Both the materials showed typical absorption bands between the wave number of 1000 and 4000 cm^{-1}. The broad absorption bands at the wave number of 3443 and 3436 cm^{-1} for HC and activated carbon, respectively, are due to O–H stretching vibrations of the surface hydroxyl groups and adsorbed water molecules. The O-H absorption peak was relatively higher on the activated sample, a factor that could be attributed to the greater availability of surface functional groups as a result of the activation by KOH. The absorption peak at around 2919 cm^{-1} represents the asymmetrical C-H stretching vibration; the decline in the intensity of this peak after the activation is an indication that hydrogen containing groups were removed during the high temperature process. The absorption peak at 1634 cm^{-1} is due to C = C stretching vibrations, while the absorption peak at about 1384 cm^{-1} is attributed to C-O stretching vibrations due to alcohols, phenols, and carboxyl functional groups [35, 43]. Apart from the previously mentioned bands, another band at 1077 cm^{-1} due to stretching vibrations of C–O was present in HC; however, it vanished post-activation, implying the removal of oxygen-containing functional groups from the material. The above-mentioned alterations in surface functional groups would assist in improving the accessibility of the electrolyte in the material.

Raman study was done in order to provide additional information on the structure of HC and activated carbon. The obtained Raman spectrum is shown in Fig. 2(d). As can be seen from the graph, both HC

and activated carbon samples have two characteristic bands, which are called D and G. Specifically, the first one (D) can be observed at 1329 cm^{-1} in HC sample and at 1341 cm^{-1} in the case of AC and the second one (G) can be observed at 1577 cm^{-1} in the case of HC and 1579 cm^{-1} in the case of activated carbon [44]. The D band reflects structural disordering, while the G band is associated with in-plane vibrations of sp^2-bonded graphitic carbon. Thus, ID/IG ratios for HC and AC were 1.44 and 1.26, respectively[45]. The decrease in the ID/IG ratio of the AC material implies that there is some enhancement in the graphitic ordering after the KOH activation, even though a porous network is formed. This means that chemical activation leads to restructuring without damaging the graphitic planes for electronic conduction.

3.2 Electrochemical Analysis

Electrochemical properties of HC and AC samples obtained from coconut rachis in 6 M KOH, NaOH, and LiOH electrolytes were investigated to understand the effect of carbon structures and electrolyte types on the charging behavior of supercapacitors. CV measurements were carried out within the scan rate of 10 to 100 mV s^{-1} for a typical three-electrode electrochemical cell setup, where Ag/AgCl was used as reference electrode and Pt wire as counter electrode. For HC, CV measurements were performed at 1.0, 0.8, and 0.6 V potential windows in 6 M KOH, NaOH, and LiOH electrolytes, respectively, while 1.0, 0.9, and 0.8 V potential windows were measured for AC in corresponding electrolytes (Fig. 3a–f).

HC electrodes demonstrated distorted CV responses which did not follow the ideal quasi-rectangular profile in all three electrolytes, showing poor capacitive nature and slow kinetic rates of charging/discharging processes. The lack of clear rectangular CV response profile implies ineffective formation of electric double layer, which is due to the presence of compact structure, smaller specific surface area and insufficient accessibility of pores in HC. Therefore, only a portion of the electrode's surface participated in the ions' sorption process, resulting in lower capacitance of the electrode. Capacitances, derived from the areas of CV curves at the scanning rate of 10 mV s^{-1}, were equal to 60, 26, and 15 F g^{-1} in the case of electrolytes 6 M KOH, NaOH, and LiOH, correspondingly. Among the three electrolytes, HC showed the maximum capacitance value in 6 M KOH solution, while 6 M NaOH and 6 M LiOH solutions followed.[46]. Conversely, the CV profiles of the AC electrodes were almost quasi-rectangular at all scan rates, indicating capacitive characteristics due to electric double layer formation and good reversibility in charge-discharge processes. The enhanced electrochemical performance of AC can be ascribed to the highly developed porous structure and higher specific surface area of the activated carbon due to KOH activation that provides many active sites for ion adsorption and fast diffusion of the electrolyte. A schematic representation of electrolyte ion adsorption on the surface of both HC and AC is shown in Fig. 4. At a scan rate of 10 mV s^{-1}, the activated carbon delivered specific capacitances of 201, 88, and 61 F g^{-1} in 6 M KOH, NaOH, and LiOH electrolytes, respectively. As the scan rate increased from 10 to 100 mV s^{-1}, the specific capacitance gradually decreased for all electrolytes because the electrolyte ions had insufficient time to diffuse into the internal pore network and fully utilize the available active sites, thereby reducing the charge-storage capability at higher scan rates [47, 48]. The variation in specific capacitance with different concentrations of electrolyte is given in Table 2. Both

HC and AC exhibited the highest capacitance in 6 M KOH, followed by 6 M NaOH and 6 M LiOH. The superior electrochemical performance observed in KOH can be attributed to the smaller hydrated ionic radius (3.31 Å) and higher ionic conductivity (73.5 S cm^2 mol^{-1}) of K^+ compared with Na^+ (3.58 Å and 50.11 S cm^2 mol^{-1}) and Li^+ (3.82 Å and 38.69 S cm^2 mol^{-1})[49, 50]. The small-sized K^+ ions can easily diffuse through the network of pores and reach more active electrochemical sites, and their higher ionic conductivity allows for quicker charge transportation within the electrolyte [51]. In the case of Na^+ and Li^+, their bigger radii and low ionic conductivities hamper the diffusion of the ions and thus lead to poor utilization of the porous electrode and low specific capacitance. To study the charge storage characteristics and rate performance of HC and AC in various alkaline electrolytes, galvanostatic charge discharge (GCD) tests were conducted at different current densities. The relevant GCD graphs are shown in Fig. 5(a-f).

Table 2
Comparison of the specific capacitance of HC and AC electrodes in different 6 M alkaline electrolytes.

Material	Electrolyte	Specific Capacitance (F g^{-1})
Hard carbon (HC)	6 M KOH	60
Hard carbon (HC)	6 M NaOH	26
Hard carbon (HC)	6 M LiOH	15
Activated carbon (AC)	6 M KOH	201
Activated carbon (AC)	6 M NaOH	88
Activated carbon (AC)	6 M LiOH	61

The galvanostatic charge–discharge (GCD) behavior of both HC and AC samples was studied at the current densities of 1 to 10 A g^{-1} in the potential windows used in the CV tests, and the resulting GCD curves are shown in Fig. 5(a–f). The HC electrodes exhibited relatively short charge–discharge durations in all three electrolytes, indicating limited charge-storage capability. The nearly symmetric triangular profiles suggest predominantly electric double-layer capacitive behaviour, while the short discharge times reflect the comparatively low specific capacitance of HC. The specific capacitances of HC in the electrolyte of 6 M KOH, NaOH, and LiOH at the current density of 1 A g^{-1} were determined using the discharge curves as 59, 25, and 15 F g^{-1}, respectively. In turn, the electrodes fabricated from AC had much larger and symmetrical GCD profiles, which confirmed better ability to store charges and good electrochemical reversibility. The prolonged discharge is explained by the high porosity structure and high specific surface area of activated carbon that gives a large number of adsorption centers for electrolyte ions. Consequently, the activated carbon delivered specific capacitances of 199, 71, and 55 F g^{-1} in 6 M KOH, NaOH, and LiOH, respectively, at a current density of 1 A g^{-1} [52].

To further understand the electrochemical behaviour of HC and AC in different alkaline electrolytes, electrochemical impedance spectroscopy (EIS) measurements were performed over a frequency range

of 0.01 Hz to 10^5 Hz, and the corresponding Nyquist plots are presented in Fig. 6(a). The activated carbon electrode exhibited a small semicircular feature in the high-frequency region, indicating a relatively low charge-transfer resistance and efficient charge transport at the electrode/electrolyte interface [53, 54]. In contrast, the HC electrode showed an indistinct or nearly absent semicircle, reflecting its comparatively poorer charge-transfer characteristics. The bulk resistance (Rb), corresponding to the electrolyte resistance between the working and reference electrodes, was determined to be 0.13 Ω, 0.74 Ω, and 0.61 Ω in 6 M KOH, NaOH, and LiOH electrolytes, respectively. Of all the electrolytes tested, 6 M KOH showed the least value of bulk resistance, implying that it has better ionic conductivity and ion transfer inside the carbon electrode. This can be attributed to its higher ionic conductivity.

Bode phase plots for HC and AC in various alkaline electrolytes have been presented in Fig. 5(c–f). Maximum phase angle was seen to be of approximately 60° in case of the HC electrode, indicating deviation from ideal capacitive behaviour. On the other hand, AC electrode in 6 M KOH electrolyte has shown a phase angle of 80° that is very close to the ideal capacitive behaviour of 90°, showing excellent charge storage capacity and faster ion transportation[55, 56]. The comparatively lower phase angles observed in NaOH and LiOH electrolytes further confirm their reduced capacitive performance. The results of EIS are consistent with the observations from CV and GCD experiments, which prove that the porous structure of AC and better ionic conductivity of KOH electrolyte result in effective charge transfer.Figure 5. (a) Variation in capacitance with current density ranging from 1–10 A⋅g^{-1} for HC and AC in different electrolytes (b) Nyquist plot of HC and AC from coconut rachis in the dissimilar electrolyte, (c-h) Bode plots in HC and AC in 6M KOH, NaOH and LiOH electrolytes

3.3 Electrochemical properties of Symmetric supercapacitor

Electrochemical properties of the symmetric supercapacitor made from coconut rachis-activated carbon with respect to 6M KOH electrolyte have been successfully understood via CV, GCD, and EIS studies. CV measurements performed on the device were conducted within a potential range of 0.7V with scan rates varying between 0.01 and 0.5 V/s (Fig. 6(a)). Absence of any redox peaks in the CV curves proves the working principle of the device is based on double-layer charge storage, which is an ideal capacitive behavior [57]. Specific capacitance value obtained from the area of the CV curve was found to be 35.40 F·g^{-1} at a slower scan rate of 0.01 V⋅s-1, indicating a highly efficient charge storage ability of the material at a lower scan rate. Another evidence of ideal capacitive nature of the device comes from the symmetric triangular shape of the GCD curve measured within a current density range of 0.1 A·g^{-1} to 1 A·g^{-1} (Fig. 6(b). The calculated capacitance value through the GCD analysis was consistent with the results of CV analysis, thus boosting the credibility of the results. In addition, the energy density value of 2.41 Wh·kg^{-1} was attained by the device, which indicated its applicability for energy purposes. In addition, EIS analysis also had a relatively small charge transfer resistance value (Rct) of 0.78 Ω and bulk resistance (Rb) of 0.41 Ω, which showed good ion mobility with less resistive losses, thus enhancing the

electrochemical properties of the device, Fig. 6(c). Cyclic stability of the device was investigated over 2000 cycles through the GCD analysis at 1 $A \cdot g^{-1}$, and the capacitance decreased from 20.5 to 19.1 $F \cdot g^{-1}$ (Fig. 6(d)), implying ~ 93% capacitance retention. These results clearly confirm the high efficiency and good energy storage capability of the coconut rachis-activated carbon in supercapacitors.

Conclusions

The present investigation clearly indicates that the performance of the coconut rachis-based carbon materials is mainly dependent on their structural characteristics. The chemical activation with KOH changed the hard carbon with dense structure to highly porous activated carbon with high specific surface area (~ 1025 $m^2\ g^{-1}$), which facilitated good electrolyte ion transportation as well as provided sufficient electrochemically active sites. As a result, the activated carbon showed better capacitive behaviour than the hard carbon in all types of the electrolytes studied. In particular, the 6 M KOH was found to provide the highest specific capacitance of 201 F g^{-1} due to the high ionic conductivity as well as low hydrated radius of K^+ ions. Moreover, the supercapacitor fabricated from the activated carbon had the specific capacitance of 35.4 F g^{-1}, energy density of 2.41 Wh kg^{-1}, and ~ 93% capacitance retention over 2000 charge-discharge cycles. The results obtained illustrate that optimization of the pore characteristics of biomass-based carbon is important for improving the performance of supercapacitors.

Declarations

Competing interests

The authors declare no competing interests

Author Contribution

Devu Bindhu: Prepared original draft, Conceptualization, Methodology, Formal Analysis, InvestigationM S Gayathri: Validation, Formal analysis, methodology, VisualizationAnju Ramachandran: Data curation, validation, visualizationJinchu I: Reviewing and editingRajan Jose: Supervision, Project administration, ReviewingC O Sreekala: Supervision, Reviewing and editing

Acknowledgement

The authors gratefully acknowledge Amrita Vishwa Vidyapeetham, Amritapuri Campus, India, for providing financial support, research facilities, and laboratory infrastructure to carry out this work. The authors also gratefully acknowledge the Research and Innovation Department of Universiti Malaysia

Pahang Al-Sultan Abdullah (UMPSA), Malaysia, for the financial support and research facilities provided through the First in the World research grant on "Biographite" (Grant No. RDU 223101).

Data Availability

The datasets generated during and/or analysed during the current study are available from the corresponding author on reasonable request.

References

1. Salem Algarni, V., Tirth, T., Alqahtani, S., Alshehery & Kshirsagar, P. Contribution of renewable energy sources to the environmental impacts and economic benefits for sustainable development. *Sustain. Energy Technol. Assess.* **56** 10.1016/j.seta.2023.103098 (2023).
2. Yamini Yasoda, K., Sathish Kumar, M., Kumar, S. & Batabyal Polyaniline decorated manganese oxide nanoflakes coated graphene oxide as a hybrid-supercapacitor for high performance energy storage application, *Ionics*, vol. 26, no. 5, pp. 2493–2500, (2019). 10.1007/s11581-019-03294-w
3. Seeram Ramakrishna and Rajan Jose. Principles of materials circular economy, *Matter*, vol. 5, no. 12, pp. 4097–4099, (2022). 10.1016/j.matt.2022.11.009
4. Ramakrishna, S. & Jose, R. Addressing sustainability gaps, *Sci Total Environ*, vol. 806, no. Pt 3, p. 151208, Feb 1 (2022). 10.1016/j.scitotenv.2021.151208
5. Al-Shetwi, A. Q. Sustainable development of renewable energy integrated power sector: Trends, environmental impacts, and recent challenges. *Sci. Total Environ.* **822**, 153645. 10.1016/j.scitotenv.2022.153645 (May 20 2022).
6. Ravikumar Jayabal Towards a carbon-free society: Innovations in green energy for a sustainable future. *Results Eng.* **24** 10.1016/j.rineng.2024.103121 (2024).
7. Chandra Sekharan Nair Omana Amma Sreekala & Indiramma, J. Mahesh Saran Roy Kandala Bala Subramanya Pavan Kumar and Karyaveettil Savithriamma Sreelatha, Functionalized multi-walled carbon nanotubes for enhanced photocurrent in dye-sensitized solar cells. *J. Nanostructure Chem.* **3** (1). 10.1186/2193-8865-3-19 (2013).
8. Lekshmi, P. S., Albert, A., Jinchu, I. & Sreekala, C. O. Energy storage application of titanium doped vanadium pentoxide nanostructures prepared by electrospinning method, *Materials Today: Proceedings*, vol. 33, pp. 1420–1423, (2020). 10.1016/j.matpr.2020.06.528
9. Mohammad, K., Hassan, M., Nasser, K., Song & Al-Ejji, M. Special issue: material science for environmentally sustainable world. *Emergent Mater.* **7** (2), 355–356. 10.1007/s42247-024-00692-3 (2024).
10. Wojciech Mrozik, M. A., Rajaeifar, O., Heidrich & Christensen, P. Environmental impacts, pollution sources and pathways of spent lithium-ion batteries. *Energy Environ. Sci.* **14** (12), 6099–6121. 10.1039/d1ee00691f (2021).

11. Yue Yang, E. G. et al. On the sustainability of lithium ion battery industry – A review and perspective. *Energy Storage Mater.* **36**, 186–212. 10.1016/j.ensm.2020.12.019 (2021).
12. Muhammad Zahir Iqbal, Mian Muhammad Faisal and Syeda Ramsha Ali. Integration of supercapacitors and batteries towards high-performance hybrid energy storage devices. *Int. J. Energy Res.* **45** (2), 1449–1479. 10.1002/er.5954 (2020).
13. Kabir, O., Oyedotun, Bhekie, B. & Mamba New trends in supercapacitors applications. *Inorg. Chem. Commun.* **170** 10.1016/j.inoche.2024.113154 (2024).
14. Arindam Dutta, S., Mitra, M., Basak & Banerjee, T. A comprehensive review on batteries and supercapacitors: Development and challenges since their inception. *Energy Storage*. **5** (1). 10.1002/est2.339 (2022).
15. Naveen, T. B., Durgalakshmi, D., Balakumar, S. & Ajay Rakkesh, R. Biomass-derived vanadium-based MAX phase nanostructures as stabilizer-free materials for symmetric supercapacitors. *Emergent Mater.* **7** (6), 2381–2391. 10.1007/s42247-024-00741-x (2024).
16. Cao, C. & Yu Wu and The way to improve the energy density of supercapacitors: Progress and perspective. *Sci. China Mater.* **61** (12), 1517–1526. 10.1007/s40843-018-9290-y (2018).
17. Jiří Libich, J. & Máca Jiří Vondrák, Ondřej Čech and Marie Sedlaříková, Supercapacitors: Properties and applications. *J. Energy Storage*. **17**, 224–227. 10.1016/j.est.2018.03.012 (2018).
18. Abdel Maksoud, M. I. A. et al. Charlie Farrell, Ala'a H. and Advanced materials and technologies for supercapacitors used in energy conversion and storage: a review, *Environmental Chemistry Letters*, vol. 19, no. 1, pp. 375–439, (2020). 10.1007/s10311-020-01075-w
19. Yu, S. et al. Towards Negative Emissions: Hydrothermal Carbonization of Biomass for Sustainable Carbon Materials. *Adv. Mater.* **36** (18), e2307412. 10.1002/adma.202307412 (May 2024).
20. Kothandam, G. et al. Recent Advances in Carbon-Based Electrodes for Energy Storage and Conversion. *Adv. Sci. (Weinh)*. **10** (18), e2301045. 10.1002/advs.202301045 (Jun 2023).
21. Patel, K. K., Singhal, T., Pandey, V., Sumangala, T. P. & Sreekanth, M. S. Evolution and recent developments of high performance electrode material for supercapacitors: A review. *J. Energy Storage*. **44** 10.1016/j.est.2021.103366 (2021).
22. Devu Bindhu, J. K., Ling, I. I., Misnon, C. C. & Yang Chandrasekharan Nair Omanaamma Sreekala and Rajan Jose, Tetrahedrally Crystallized Carbon from Biowaste-Derived Microcrystalline Cellulose. *ACS Sustainable Resource Manage.* **1** (9), 2128–2135. 10.1021/acssusresmgt.4c00228 (2024).
23. Devu Bindhu, C. N. O., Sreekala, C. C., Yang & Jose, R. Biogenic Hard and Soft Carbons from Coconut Palm Waste: A Review of Structure-property Relationships for Energy Storage Devices. *Mater. Circular Econ.* **8** (1). 10.1007/s42824-026-00244-6 (2026).
24. Tasmina Khandaker, T., Islam, A. & Nandi Md Al Amin Mia Anik, Md Shihab Hossain, Md Kamrul Hasan and Muhammad Sarwar Hossain, Biomass-derived carbon materials for sustainable energy applications: a comprehensive review. *Sustainable Energy Fuels*. **9** (3), 693–723. 10.1039/d4se01393j (2025).

25. Stephanie, N. E. M. *The transition from fossil fuel as a source of energy to renewable energy* (Centria University of Applied Sciences, 2022).
26. Xianzhong Sun, X., Zhang, H., Zhang, D., Zhang & Ma, Y. A comparative study of activated carbon-based symmetric supercapacitors in Li2SO4 and KOH aqueous electrolytes. *J. Solid State Electrochem.* **16** (8), 2597–2603. 10.1007/s10008-012-1678-7 (2012).
27. Kumar, K. et al. Biomass waste-derived carbon materials for sustainable remediation of polluted environment: A comprehensive review, *Chemosphere*, vol. 345, p. 140419, Dec (2023). 10.1016/j.chemosphere.2023.140419
28. Bingbing, Q., Hu, W., Zhang, D., Wang, Y. & Chu, H. Biomass-derived carbon as a potential sustainable material for supercapacitor-based energy storage: Design, construction and application. *J. Anal. Appl. Pyrol.* **181** 10.1016/j.jaap.2024.106652 (2024).
29. Yameen, M. Z. & Naqvi, S. R. Dagmar Juchelková and Muhammad Nouman Aslam Khan, Harnessing the power of functionalized biochar: progress, challenges, and future perspectives in energy, water treatment, and environmental sustainability, *Biochar*, vol. 6, no. 1, (2024). 10.1007/s42773-024-00316-3
30. Devu Bindhu, C. O. et al. High carbon containing biomaterial offering honeycomb morphology as a charge storing electrode in aqueous alkaline electrolytes, *Journal of Electroanalytical Chemistry*, vol. 967, p. 118423, (2024). 10.1016/j.jelechem.2024.118423
31. Zhou, X., Shu, S., Ye, X. & Li, Z. Engineering Faradaic Electrode Materials for High-Efficiency Water Desalination, *Small*, vol. 20, no. 32, p. e2400047, Aug (2024). 10.1002/smll.202400047
32. Javed, M. S. et al. Tayyaba Najam and Weihua Han, The quest for negative electrode materials for Supercapacitors: 2D materials as a promising family. *Chem. Eng. J.* **452** 10.1016/j.cej.2022.139455 (2023).
33. NurulHuda, S. JinKiong Ling, Devu Bindhu, Ghufira, Izan Izwan Misnon, Chandrasekharan Nair Omanaamma Sreekala, Chun-Chen Yang and Rajan Jose, Lithium-ion storage in honeycomb-structured biomass-derived porous carbon. *Diam. Relat. Mater.* **151**, 111797. 10.1016/j.diamond.2024.111797 (2025).
34. Sam, D. K., Li, H., Xu, Y. T. & Cao, Y. Advances in porous carbon materials for a sustainable future: A review. *Adv. Colloid Interface Sci.* **333**, 103279. 10.1016/j.cis.2024.103279 (Nov 2024).
35. Devu Bindhu, B. S. et al. Effect of mass loading on the capacitive performance of sustainable porous carbon. *J. Mater. Sci.: Mater. Electron.* **36** (9). 10.1007/s10854-025-14670-w (2025).
36. Elie Sogbochi Clement Kolawolé Balogoun, Guevara Nonviho, Saka Moussiliou, Cokou Pascal Agbangnan Dossa and Dominique Codjo Koko Sohounhloue, Synthesis of porous carbons for the fixing of cationic molecules in aqueous solution. *Sci. Afr.* **25** 10.1016/j.sciaf.2024.e02332 (2024).
37. Azeem Sarwar, M. et al. Salman Raza Naqvi and Muhammad Asjid, Synthesis and characterization of biomass-derived surface-modified activated carbon for enhanced CO2 adsorption. *J. CO2 Utilization*. **46** 10.1016/j.jcou.2021.101476 (2021).

38. Fei Sun, X., Huang, L., Wang, H., Liu & Kuai, L. Biomass-derived N/O co-doped meso-microporous carbon nanosheets for high performance zinc storage. *Microporous Mesoporous Mater.* **399** 10.1016/j.micromeso.2025.113870 (2026).
39. Tian, W. et al. Porous Carbons: Structure-Oriented Design and Versatile Applications. *Adv. Funct. Mater.* **30** (17). 10.1002/adfm.201909265 (2020).
40. Rishika Chakraborty, Vilya, K. & Mukul Pradhan and Arpan Kumar Nayak. Recent advancement of biomass-derived porous carbon based materials for energy and environmental remediation applications. *J. Mater. Chem. A*. **10** (13), 6965–7005. 10.1039/d1ta10269a (2022).
41. Vaishak Sunil, A., Yasin, B., Pal, I. I., Misnon, C. & Karuppiah, C. C. Yang and Rajan Jose, Tailoring the charge storability of commercial activated carbon through surface treatment. *J. Energy Storage*. **55** 10.1016/j.est.2022.105809 (2022).
42. Zhang, C., Cao, Y., Liu, Y., Zhang, Y. W. & Hua-Jin Hu, Zhi Gen Yu and Bct-C5: A new body-centered tetragonal carbon allotrope. *Diam. Relat. Mater.* **119** 10.1016/j.diamond.2021.108571 (2021).
43. Devu & Bindhu Chandrasekharannair Omanamma Sreekala and Rajan Jose, Honeycomb-shaped biomass-derived porous carbon for removal of the heavy metal ions from domestic and industrial wastewaters. *Diam. Relat. Mater.* **157** 10.1016/j.diamond.2025.112528 (2025).
44. Vali, I. P. et al. Bamboo and coconut shell based activated carbon: A Raman spectroscopic study. *Mater. Chem. Phys.* **318** 10.1016/j.matchemphys.2024.129240 (2024).
45. Vaibhav Ganachari, P., Maldar, S. & Shirguppikar, R. A. Magdum and Alemu Workie Kebede, Synthesis and characterization of reduced graphene oxide for supercapacitors. *Results Eng.* **30** 10.1016/j.rineng.2026.110693 (2026).
46. Jian, W. et al. Enzymatic Hydrolysis Lignin-Derived Porous Carbons through Ammonia Activation: Activation Mechanism and Charge Storage Mechanism. *ACS Appl. Mater. Interfaces*, **14**, 4, pp. 5425–5438, Feb 2 2022, 10.1021/acsami.1c22576
47. Jian, W. et al. Alshareef and Xueqing Qiu, Engineering Pore Nanostructure of Carbon Cathodes for Zinc Ion Hybrid Supercapacitors. *Adv. Funct. Mater.* **32** (49). 10.1002/adfm.202209914 (2022).
48. Yuan Wang, Z., Qian, C. M., Zhang, Z., Lin, J. & Huang, F. Enhanced specific capacitance by a new dual redox-active electrolyte in activated carbon-based supercapacitors, *Carbon*, vol. 143, pp. 300–308, (2019). 10.1016/j.carbon.2018.11.033
49. Damilola Momodu, M. et al. Activated carbon derived from tree bark biomass with promising material properties for supercapacitors. *J. Solid State Electrochem.* **21** (3), 859–872. 10.1007/s10008-016-3432-z (2016).
50. Lv, Y. et al. Application of dandelion-like Sm(2)O(3)/Co(3)O(4)/rGO in high performance supercapacitors, *RSC Adv*, vol. 14, no. 3, pp. 2088–2101, Jan 3 (2024). 10.1039/d3ra06352f
51. Pal, B., Yang, S., Ramesh, S., Thangadurai, V. & Jose, R. Electrolyte selection for supercapacitive devices: a critical review. *Nanoscale Adv*, **1**, 10, pp. 3807–3835, Oct 9 2019, 10.1039/c9na00374f
52. Qu, Q. T. et al. Study on electrochemical performance of activated carbon in aqueous Li2SO4, Na2SO4 and K2SO4 electrolytes. *Electrochem. Commun.* **10** (10), 1652–1655.

10.1016/j.elecom.2008.08.020 (2008).

53. Medagedara, A. D. T. et al. Triethylammonium thiocyanate ionic liquid electrolyte-based supercapacitor fabricated using coconut shell-derived electronically conducting activated charcoal electrode material. *J. Energy Storage*. **55, p.** (105628). 10.1016/j.est.2022.105628 (2022).
54. Mousumi Bora, D. et al. Blending of Activated Low-Grade Coal Powder with Coconut Shell Waste for Supercapacitor Applications. *Energy Fuels*. **36** (23), 14476–14489. 10.1021/acs.energyfuels.2c03010 (2022).
55. Teressa, N. W. et al. Matthias Georg Schwab and Rolf Mülhaupt, 3D Micro-Extrusion of Graphene-based Active Electrodes: Towards High-Rate AC Line Filtering Performance Electrochemical Capacitors. *Adv. Funct. Mater.* **24** (29), 4706–4716. 10.1002/adfm.201304151 (2014).
56. Sahu, V., Marichi, R. B., Singh, G. & Sharma, R. K. Hierarchical Polyaniline Spikes over Vegetable Oil derived Carbon Aerogel for Solid-State Symmetric/Asymmetric Supercapacitor. *Electrochim. Acta*. **240**, 146–154. 10.1016/j.electacta.2017.04.058 (2017).
57. Manimekala, T., Sivasubramanian, R., Dar, M. A. & Dharmalingam, G. Crafting the architecture of biomass-derived activated carbon via electrochemical insights for supercapacitors: a review. *RSC Adv*, **15**, 4, pp. 2490–2522, Jan 23 2025, 10.1039/d4ra07682f

Figures

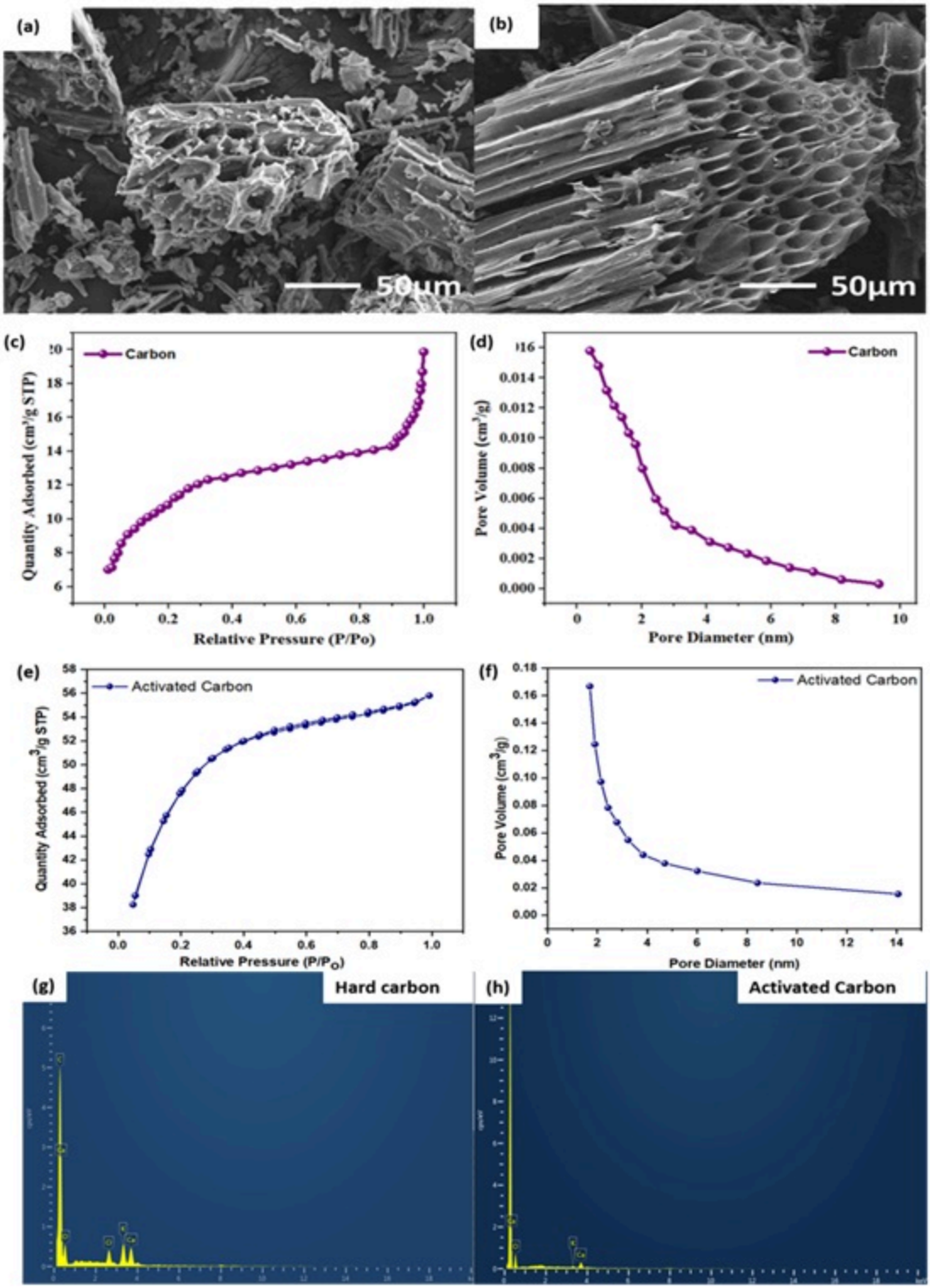

Figure 1

SEM images of coconut rachis (a) HC, 50µm (b) AC, 50µm, (c) Nitrogen adsorption–desorption curve for HC based on the BET method, (d) pore size distribution curve, (e) Nitrogen adsorption–desorption curve for AC based on the BET method, (f) pore size distribution curve, (g &h) EDAX analysis of HC and AC

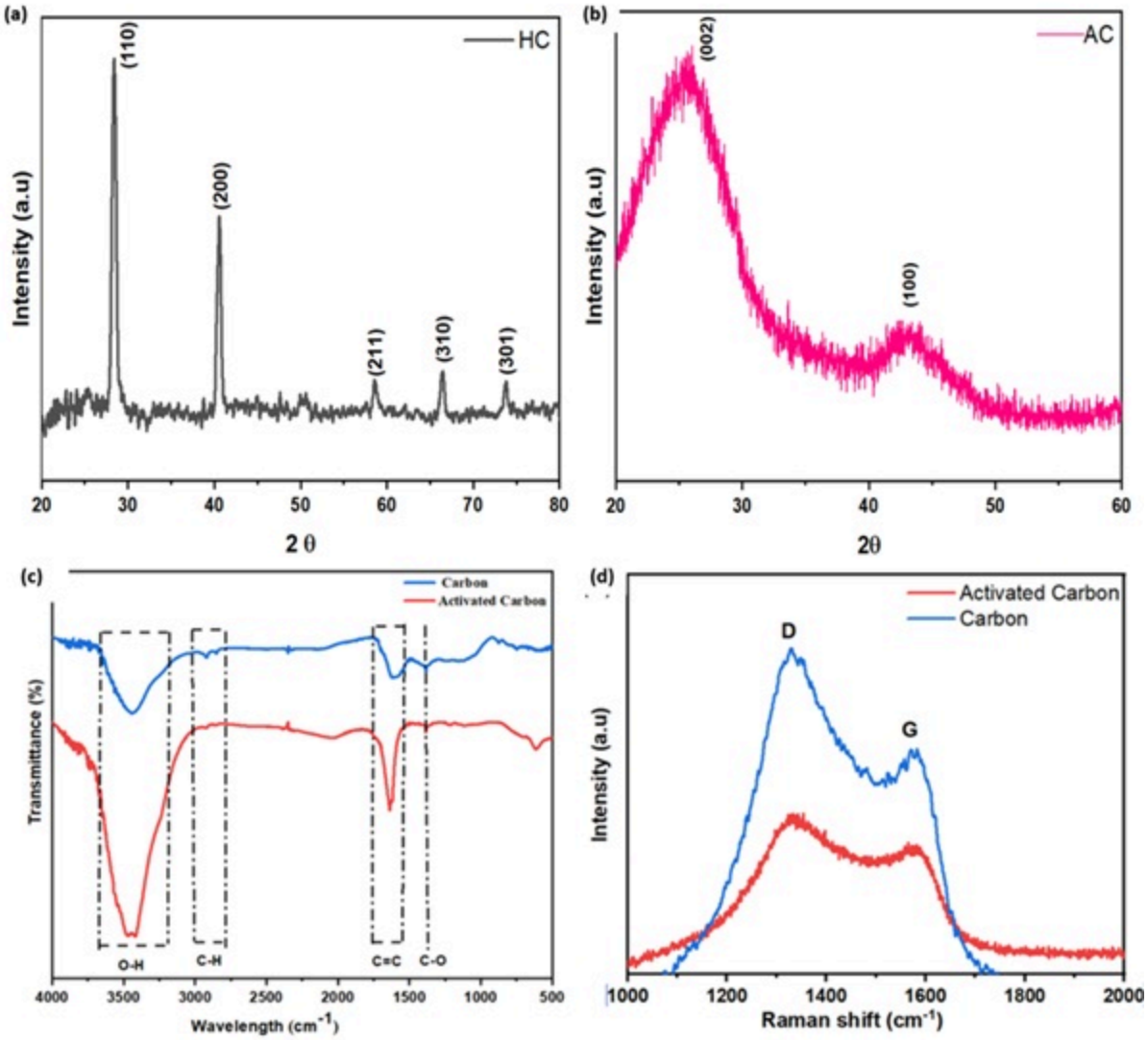

Figure 2

Structural characterization of HC and AC (a) XRD pattern of HC, (b) XRD pattern of AC, (c) FTIR spectra of HC and AC, and (d) Raman spectra of HC and AC

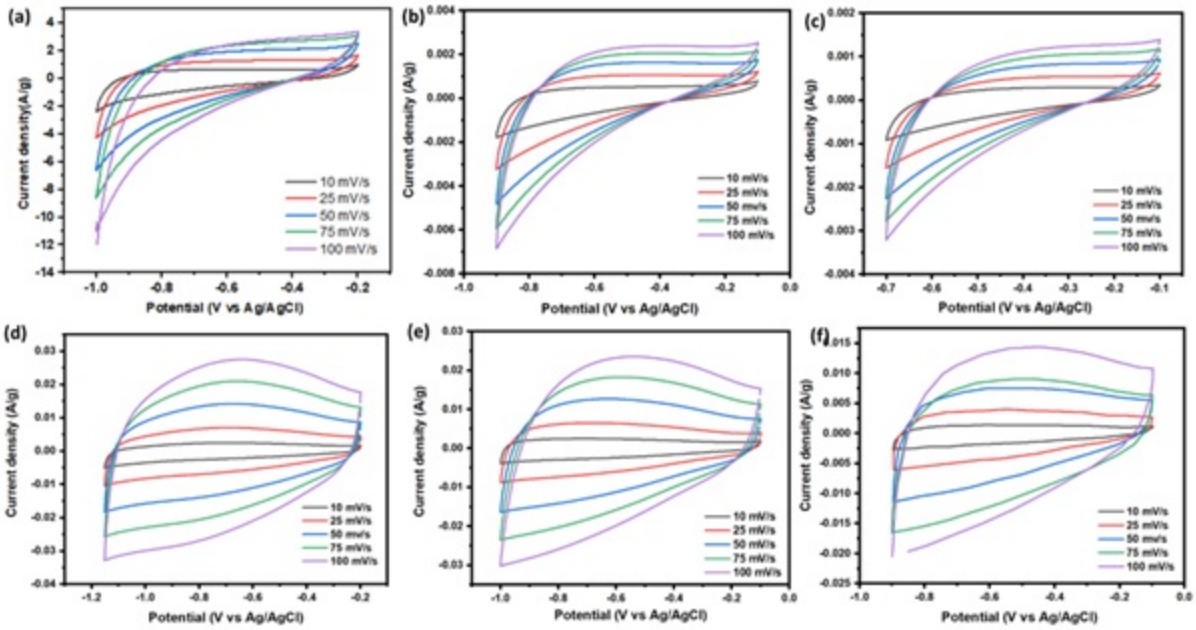

Figure 3

CV curves of coconut rachis HC in 6M (a) KOH, (b) NaOH, (c) LiOH, coconut rachis-derived AC in 6M (d) KOH, (e) NaOH and (f) LiOH electrolytes

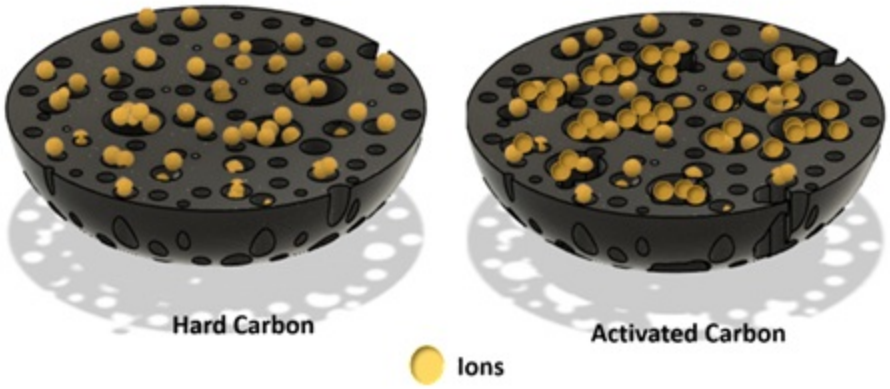

Figure 4

Schematic representation of electrolyte ion adsorption on the surface of both HC and AC. The large pore size on the HC leads to reduced ion adsorption compared to AC with a small pore size

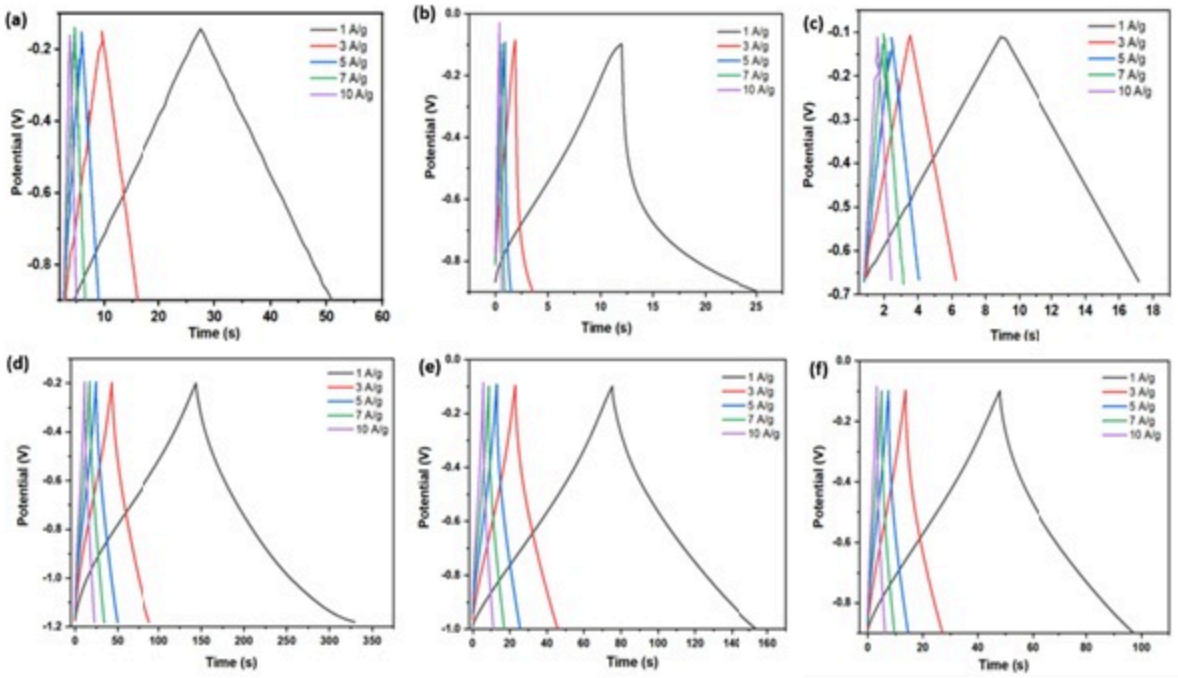

Figure 5

GCD curve of coconut rachis hard carbon electrode in 6M (a) KOH, (b) NaOH, (c) LiOH, GCD curve of coconut rachis activated carbon in 6M (d) KOH, (e) NaOH and (f) LiOH

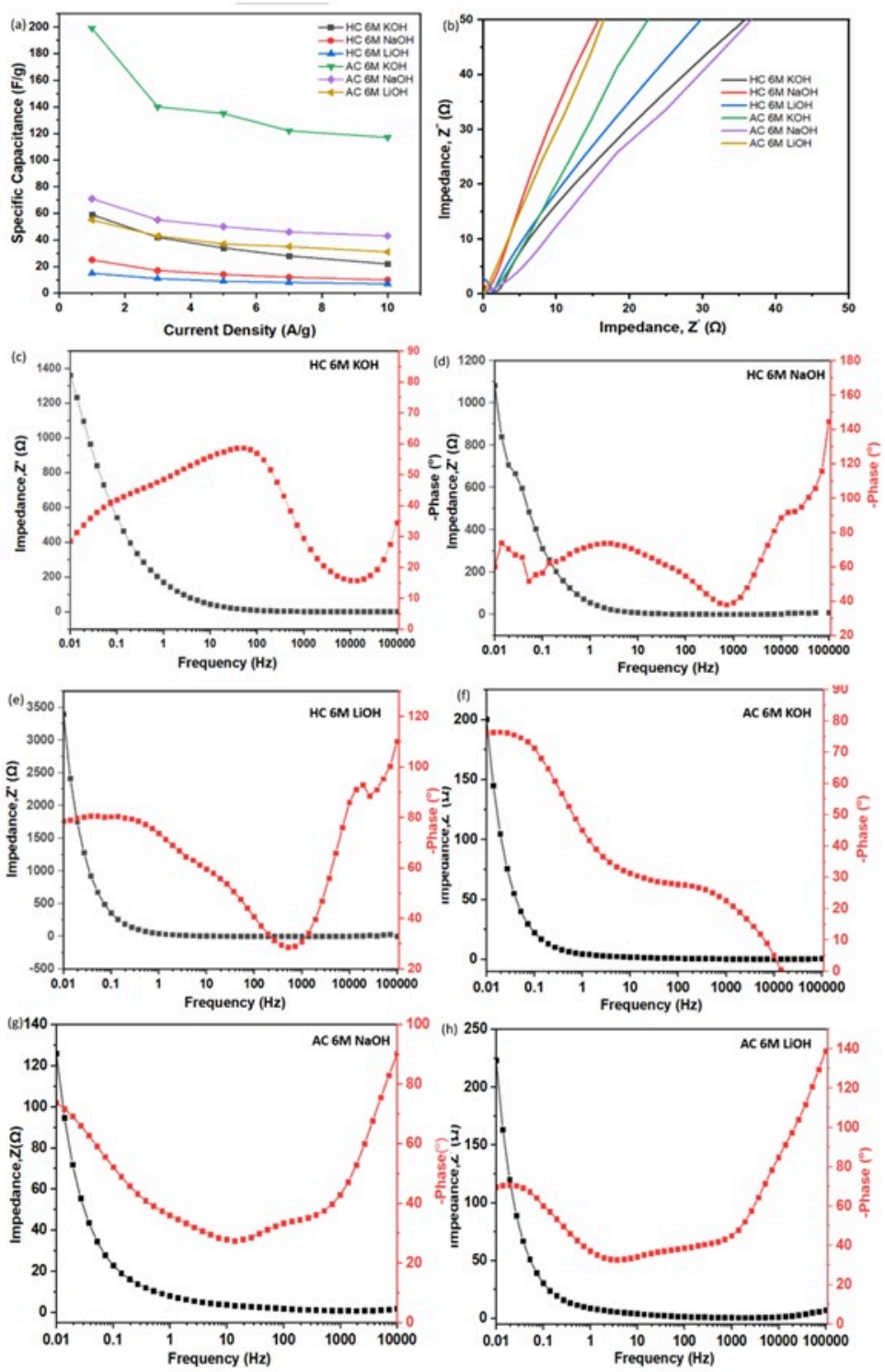

Figure 6

(a) Variation in capacitance with current density ranging from 1-10 A⋅g^{-1} for HC and AC in different electrolytes (b) Nyquist plot of HC and AC from coconut rachis in the dissimilar electrolyte, (c-h) Bode plots in HC and AC in 6M KOH, NaOH and LiOH electrolytes

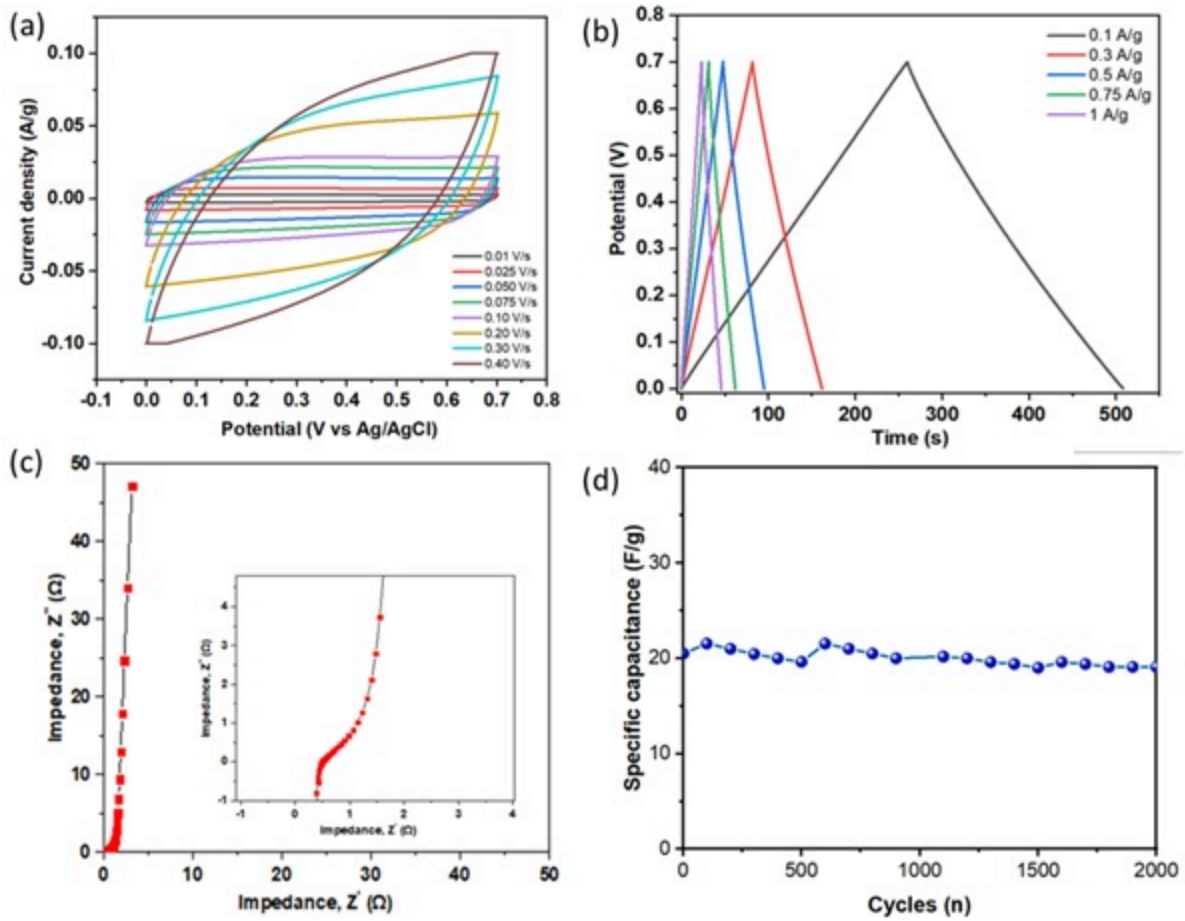

Figure 7

Symmetric supercapacitor performance in 1M NaOH electrolyte (a) CV curve, (b) GCD analysis, (c) Nyquist plot, (d) specific capacitance variation after 2000 cycles.

Supplementary Files

This is a list of supplementary files associated with this preprint. Click to download.

- Highlights.docx
- GraphicalAbstract.jpg